NANO COMMENTARY　　　　　　　　　　　　　　　**Open Access**

Multifunctional application of PVA-aided Zn–Fe–Mn coupled oxide nanocomposite

Buzuayehu Abebe[*] , H. C. Ananda Murthy[*] and Enyew Amare Zereffa

Abstract

Zinc oxide (ZnO) is a fascinating semiconductor material with many applications such as adsorption, photocatalysis, sensor, and antibacterial activities. By using a poly (vinyl alcohol) (PVA) polymer as a capping agent and metal oxides (iron and manganese) as a couple, the porous PVA-aided Zn/Fe/Mn ternary oxide nanocomposite material (PTMO-NCM) was synthesized. The thermal, optical, crystallinity, chemical bonding, porosity, morphological, charge transfer properties of the synthesized materials were confirmed by DTG/DSC, UV–Vis-DRS, XRD, FT-IR, BET, SEM-EDAX/TEM-HRTEM-SAED, and CV/EIS/amperometric analytical techniques, respectively. The PTMO-NCM showed an enhanced surface area and charge transfer capability, compared to ZnO. Using the XRD pattern and TEM image analysis, the crystalline size of the materials was confirmed to be in the nanometer range. The porosity and superior charge transfer capabilities of the PTMO-NCM were confirmed from the BET, HRTEM (IFFT)/SAED, and CV/EIS analysis. The adsorption kinetics (adsorption reaction/adsorption diffusion) and adsorption isotherm test confirmed the presence of a chemisorption type of adsorbate/methylene blue dye-adsorbent/PTMO-NCM interaction. The photocatalytic performance was tested on the Congo red and Acid Orange-8 dyes. The superior ascorbic acid sensing capability of the material was understood from CV and amperometric analysis. The noble antibacterial activities of the material were also confirmed on both gram-negative and gram-positive bacteria.

Keywords: Porous ternary nanocomposite, Adsorption, Photocatalysis, Antibacterial activity, Sensor, Mechanisms

Introduction

Zinc oxide nanoparticles (NPs) are commonly used in several fields such as adsorption [1], photocatalysis [2, 3], food preservation [4], and pollutant sensor [5]. Compared to TiO_2, the production cost of ZnO is approximately 75% lower and has higher absorption efficacy across a large fraction of the solar spectrum [6, 7]. The application of single metal oxide as a photocatalyst is restricted on the charger transfer property due to the photogenerated electron/hole recombination. This recombination, particularly in the nanosized range, leads to the diminution of their quantum efficiency and also may lead to the dissipation of radiant energy by initiating highly desirable reactions [8, 9]. Among several efforts

applied to reduce the electron–hole recombination problem such as doping, heterojunction, dye sensitization, noble and non-noble metal deposition, forming heterostructure materials was found to be one of the noble preferences [10–12]. Coupling of ZnO with other metal oxides was reported for remediation of the mentioned recombination problem [8, 13–16]. Due to their stability and unique properties, the hematite (α-Fe_2O_3) [8, 14] and Mn_2O_3 [13] are suggested to act as a decent couple with ZnO.

Besides, PVA polymer as a stabilizing agent also has great use in diminishing the electron–hole recombination problems [17]. As reported [18, 19], 500 °C is the optimum temperature to remove unwanted impurities including the PVA polymer after acting as a capping agent. Modifying the synthesized materials to have a mesoporous property that allows a rapid charge transfer process has been also reported [20, 21]. Using only environmentally benign water as a solvent and developing an

*Correspondence: buzea8@gmail.com; anandkps350@gmail.com
Department of Applied Chemistry, School of Applied Natural Science, Adama Science and Technology University, P O Box 1888, Adama, Ethiopia

Abebe *et al. Nanoscale Res Lett*   (2021) 16:1

Page 2 of 9

efficient synthesis procedure, the toxicity, cancer-causing ability, and mutagenic properties of organic solvents can also be removed.

A small variation in the standard level of ascorbic acid creates a lot of diseases in human beings [16]. As reported [22], ascorbic acid has a major role in the physiological normal functioning of organisms and also used as a treatment for a different illness. Therefore, it is significant to develop novel methods used for measuring the level of ascorbic acid. Nowadays, metal oxide nanomaterials have been largely employing as sensor applications [23]. Among several techniques that have been made to improve the sensing properties of ZnO, forming a composite with other metal oxides and modifying the synthesized materials to have a mesoporous property that allows a rapid charge transfer process have been reported [20, 21]. Furthermore, hospital-acquired infections caused by microorganisms are becoming worldwide problems [24]. ZnO is also listed as an antimicrobial agent and safe material for food preservation of foodborne diseases by the US FDA (21CFR182.8991) [4, 25].

Considering all the mentioned aspects of aggregation/agglomeration, surface area-to-volume ratio, and toxicity of organic solvents, this work synthesizes PVA-assisted PTMO-NCM using a simple sol–gel followed by accidental self-propagation techniques. The as-synthesized material was characterized by DTG/DSC, XRD, BET, SEM–EDX/TEM/HRTEM/SAED, and CV/EIS/amperometric analytical techniques. A pronounced surface area and charge transfer capability improvement have been achieved for PTMO-NCM, compared to ZnO. The applicability of the synthesized coupled PTMO-NCM was tested on adsorption and degradation of organic dyes, antibacterial activity, and an ascorbic acid sensor.

Materials and methods

The instrumental details and the reagents used were present as supplementary material (S). The detailed ZnO and PTMO-NCM synthesis procedures were also present in the author's earlier works [1, 26–28]. Roughly, the PVA polymer was dissolved in distilled water with continuous stirring on a magnetic stirrer at ~ 115 °C for about 15 min. Then, the salt precursors, $Zn(NO_3)_2.6H_2O$, $Fe(NO_3)_3.9H_2O$, and $MnSO_4.H_2O$ were mixed with previously dissolved and cooled PVA polymer solution with continuous stirring. After two days of aging followed by drying in an oven at about 110 °C, the product was gently crushed to reduce the highly amorphous self-propagated material. Finally, it was calcined at the DTG-optimized calcination temperature of 500 °C for 3 h. The calcination process at the optimized temperature helps for removing unwanted impurities as well as the PVA polymer. The synthesized PTMO-NCM was used for continuous
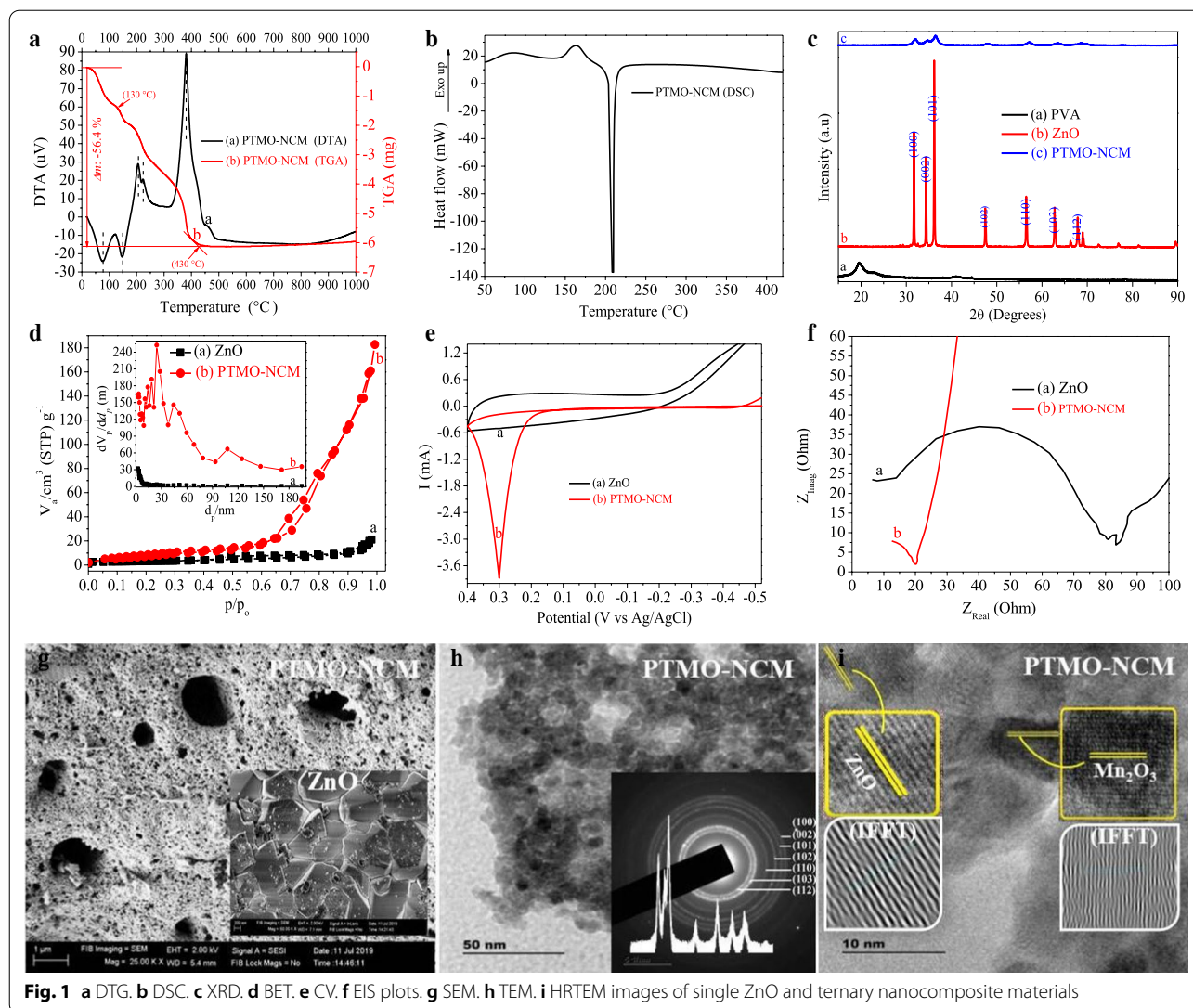
sample characterization and application tests. The photocatalytic experiment was performed using a 176.6-cm^2 circular glass reactor under a 125-W mercury vapor lamp. The 20 ppm of 250 mL Congo red (CR) and Acid Orange-8 (AO8) dyes and 0.06 g of PTMO-NCM photocatalyst were used during the experiment. The adsorption test was conducted using the experimentally optimized [1] adsorption parameters, 10–150-min adsorbate–adsorbent contact time, and 1–35 mg L^{-1} concentrations with a constant 140 rpm shaking speed. The antibacterial activity test had conducted using three different concentrations (75, 100, and 125 μg mL^{-1}) of ZnO and PTMO-NCM. The experiment was accompanied by a disk diffusion method using a 0.5 McFarland standard.

Results and discussion

Characterization results

The optimum calcination temperature was determined to be 500 °C using DTG stability analysis at a 50 °C min^{-1} flow rate of nitrogen gas. About 56% of the sample decomposition took place and left with ~ 42% of pure PTMO-NCM (Fig. 1a). From the DSC plot (see Fig. 1b), the two exothermic peaks are supposed to be due to the evaporation of adsorbed volatile components at 80 °C and conformational changes at 144 °C. The third endothermic peak that appeared at about 210 °C is probably due to the phase transformation of other forms of iron or/and manganese oxides to the stable Fe_2O_3 and Mn_2O_3 phase. Compared to ZnO, the high reflectance drop in the visible region for PTMO-NCM was observed from UV–Vis-DRS spectroscopic analysis (Additional file 1: Fig. S1a). This optical analysis supports the peak intensity reduction of the XRD pattern and the porosity interpretation of the SEM image. The Kubelka–Munk plots [29, 30] showed the nonexistence of bandgap change between ZnO and PTMO-NCM (Additional file 1: Fig. S1b).

The noticeable approximate average crystalline size reduction (6×) was obtained for PTMO-NCM, compared to ZnO (Fig. 1c). The XRD pattern peaks of both ZnO and PTMO-NCM are consistent with the hexagonal ZnO phase (ICSD: 00-036-1451, P63mc (#186-1) space group). This is probably due to the smaller percentages of iron (5%) and manganese (5%) oxides. The absence of PTMO-NCM peaks shift relative to ZnO also shows the non-appearance of structural distortion on ZnO lattice. This may indicate the presence of only a local heterojunction between the ternary metal oxides [8, 31, 32]. The XRD data and the respective size of the particles were calculated using Debye–Scherrer's formula ($D = K\lambda / (\beta\cos(\theta))$), where λ is the wavelength of X-ray radiation (for Cu 0.15418 nm), K is constant close to unity, β is the full width at half maximum (FWHM) in 2θ scales and θ is the angle of the considered Bragg reflection [33, 34].

Fig. 1 **a** DTG. **b** DSC. **c** XRD. **d** BET. **e** CV. **f** EIS plots. **g** SEM. **h** TEM. **i** HRTEM images of single ZnO and ternary nanocomposite materials

Compared to ZnO, the great surface area enhancement for PTMO-NCM (15×) and the porous nature of PTMO-NCM was approved from the BET and SEM image analysis, respectively (see Fig. 1d, g, (the inset image in Fig. 1g is for ZnO)). As per IUPAC classifications, among six types of adsorption isotherms (I–VI) and four types of the hysteresis loops, the BET plots of ZnO and PTMO-NCM look a typical IV isotherm and an H3 hysteresis loop. The approximate average BJH pore size distribution for ZnO and PTMO-NCM was determined to be 9 and 26, respectively, which is consistent with the mesoporous range of IUPAC classification [35]. The greater current rise in CV analysis [36] (Fig. 1e) and the smaller semicircle diameter of the Nyquist plot in EIS techniques [37] (Fig. 1f) confirm the enhanced charge transfer capabilities of PTMO-NCM over ZnO. The nanometer range crystalline size of the PTMO-NCM was further confirmed from the TEM image (Fig. 1h). The predictable composition and actuality of the PTMO-NCM were characterized by EDX (see Additional file 1: Fig. S2) and HRTEM analysis (Fig. 1i and its insets), respectively. The d-spacing values (0.2864, 0.2543, 0.1969, 0.1663, 0.1520, 0.1419, and 0.1104) that was determined from SAED rings (Fig. 1h inset) are also matching with XRD pattern result. The stacking faults on the HRTEM (IFFT) image and the nonexistence of the diffraction spots in the SAED ring that confirms the crystallinity of the materials [38] further confirms the porous nature of the PTMO-NCM.

Methylene blue dye adsorption

The optimized 0.02 g dosage, pH of 8, and a constant 140 rpm shaking speed were used for the

Abebe *et al. Nanoscale Res Lett*   (2021) 16:1
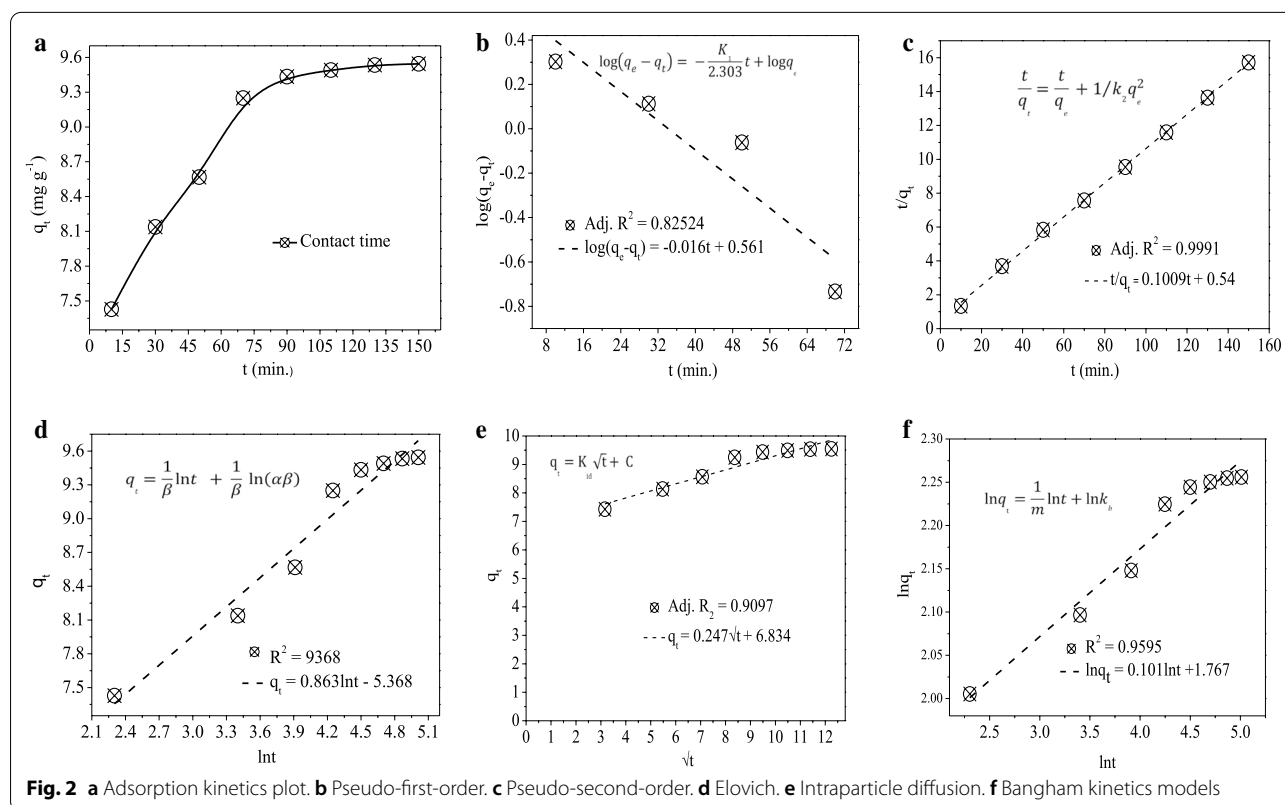
Page 4 of 9

adsorption-reaction and adsorption-diffusion kinetics studies [1]. The coefficient of determination (R^2) value and equations used to calculate the adsorption kinetics models parameter was given in the respective plots as inset (Fig. 2). Among the pseudo-first-order (PFO) (Fig. 2b), pseudo-second-order (PSO) (Fig. 2c), and Elovich (Fig. 2d) adsorption-reaction models, the PSO model that confirms the chemisorption types of adsorption fits well. Also, the theoretical (9.43 mg g^{-1}) and experimental (9.91 mg g^{-1}) values of the PSO model have a close relation unlike that of the PFO that has the experimental values of (3.64 mg g^{-1}). The intraparticle diffusion (IPD) model seems fitting well (Fig. 2e); however, to say the reaction is under the control of adsorption-diffusion, its linear plot should pass through the origin. The IPD plot for this work is not passing through the origin. From this, it is possible to conclude that the reaction is dominantly under the control of adsorption-reaction. However, the well-fitting of the Bangham model (Fig. 2f) is indicating the presence of pore diffusion in the adsorption process [39]. The presence of this pore diffusion is also consistent with the BET and SEM interpretations.
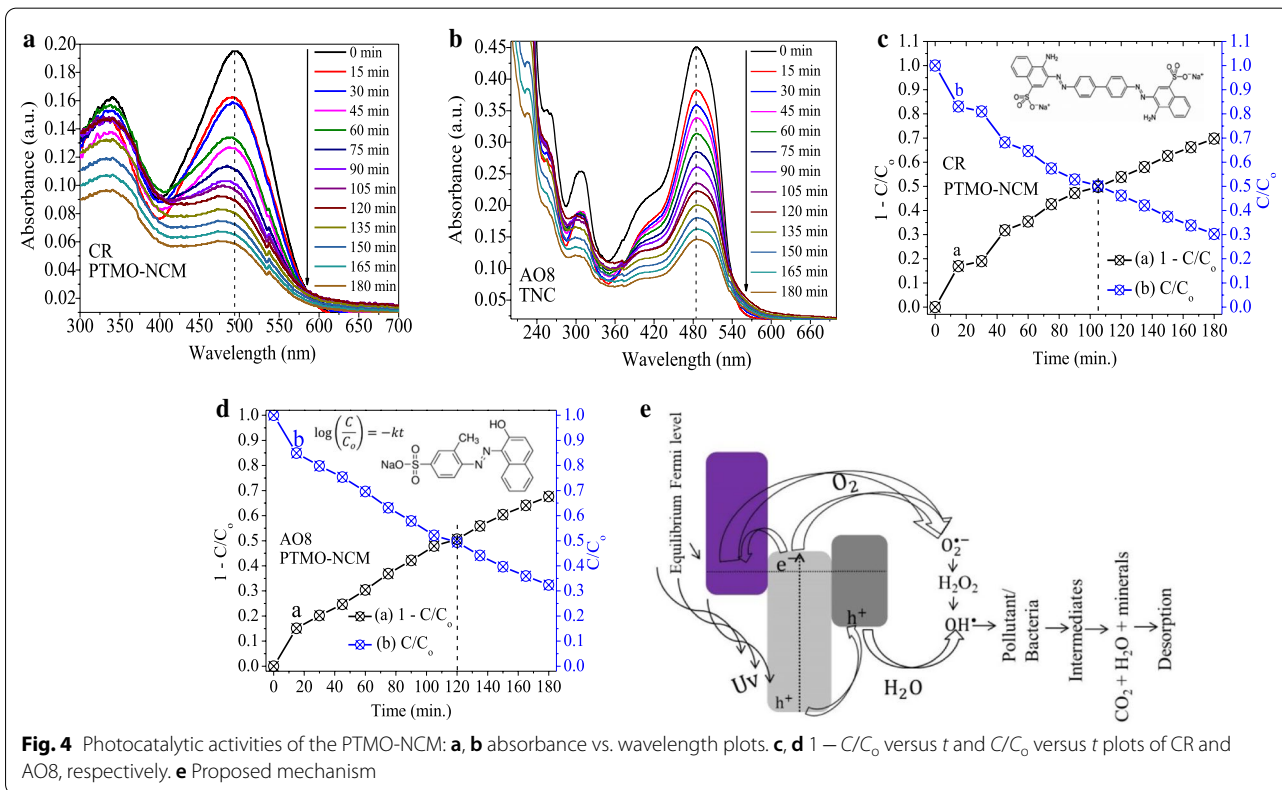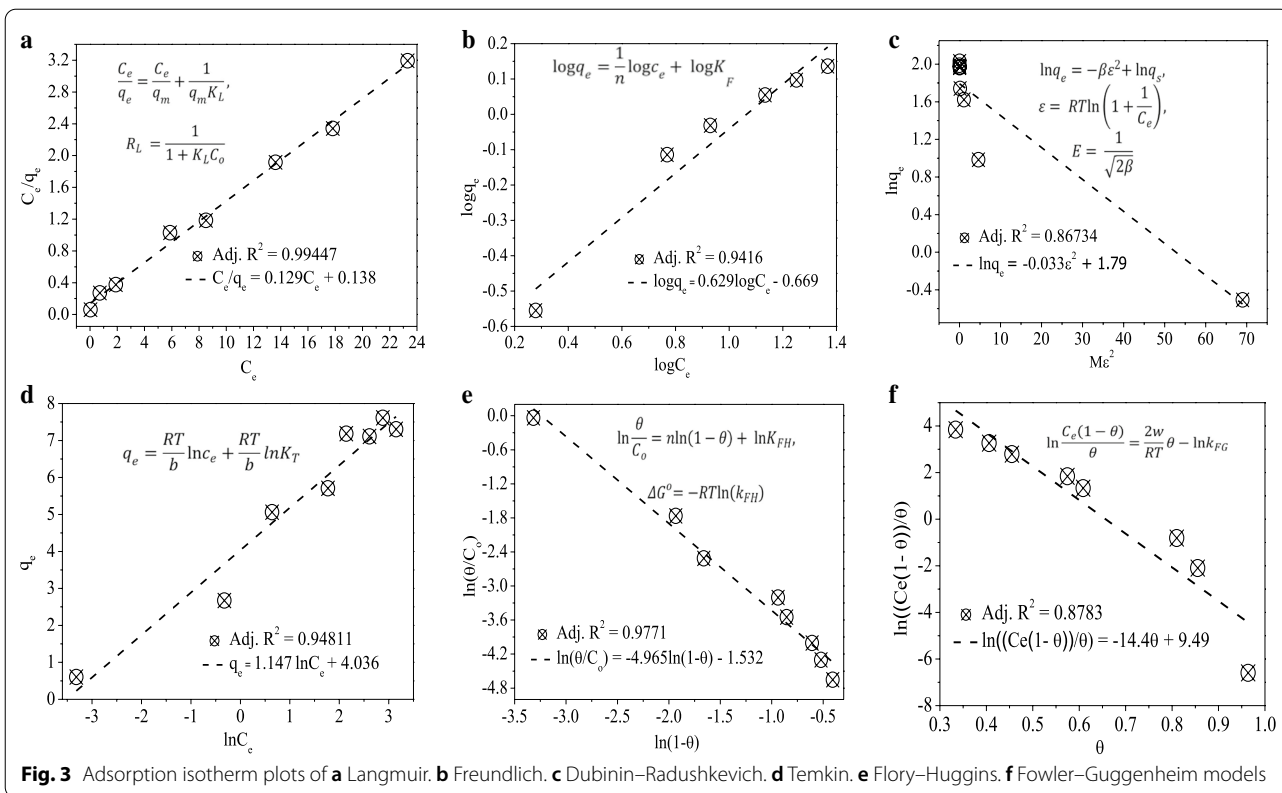
The R^2 value and equations used to calculate the adsorption isotherm models parameter were also given in the respective plots as inset (Fig. 3). Depending on the R^2 values of the adsorption isotherm models (Langmuir (Fig. 2a), Freundlich (Fig. 2b), Dubinin–Radushkevich (D–RK) (Fig. 2c), Temkin (Fig. 2d), Flory–Huggins (FH) (Fig. 2e), and Fowler–Guggenheim (FG) (Fig. 2f)), the Langmuir and FH models are showing relatively better fitting. From the Langmuir model, lying the separation factor R_L value between 0 and 1 (0.05) indicates the favorability of the adsorption process. The favorability of the adsorption process was also further confirmed from the n (1.59) value of the Freundlich model. The well-fitting of the Langmuir model indicates the presence of a monolayer methylene blue dye coverage, which is consistent with the PSO kinetics model interpretation. The maximum adsorption capacity of the adsorbent that was determined from the Langmuir isotherm model is 7.75 mg g^{-1}. The indication of the characteristic surface coverage and spontaneity of the reaction (-3.8 kJ mol^{-1}) were also deduced from the FH model equation.

Congo red and Acid Orange-8 dye degradation and mechanism

The photodegradation capabilities of PTMO-NCM were studied on the decolorization of CR and AO8 dyes at a maximum absorption wavelength of 494 and 484 nm (Fig. 4a, b), respectively. In the first 15 min, approximately 17% of CR dye and 15% of AO8 dye degradation took place. At 180 min, the maximum degradation of 70%
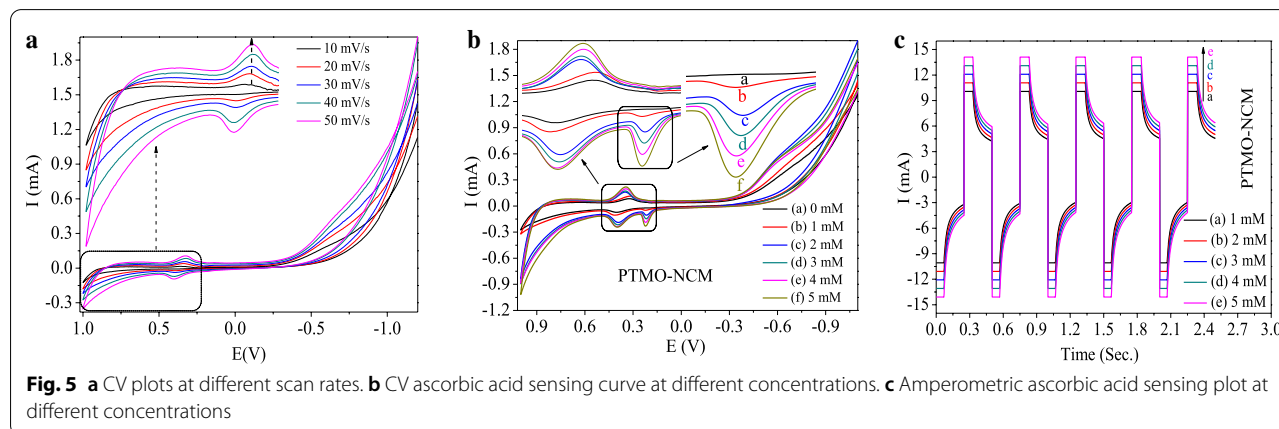

Fig. 2 **a** Adsorption kinetics plot. **b** Pseudo-first-order. **c** Pseudo-second-order. **d** Elovich. **e** Intraparticle diffusion. **f** Bangham kinetics models

Abebe *et al. Nanoscale Res Lett*   (2021) 16:1

Page 5 of 9

Fig. 3 Adsorption isotherm plots of **a** Langmuir. **b** Freundlich. **c** Dubinin–Radushkevich. **d** Temkin. **e** Flory–Huggins. **f** Fowler–Guggenheim models

Fig. 4 Photocatalytic activities of the PTMO-NCM: **a**, **b** absorbance vs. wavelength plots. **c**, **d** $1 - C/C_o$ versus t and C/C_o versus t plots of CR and AO8, respectively. **e** Proposed mechanism

for CR dye and 68% for AO8 dye was taking place. The obtained equilibrium constant k values for CR and AO8 dyes were 0.007141 and 0.005627 min^{-1}, respectively. From the contact point of $1 - C/C_o$ versus t and C/C_o versus t plots (see Fig. 4c, d), the obtained degradation half-life value was approximately 105 min for CR and 119 min for AO8. See the PFO kinetic equation used to study reaction dynamics in Fig. 4d inset.
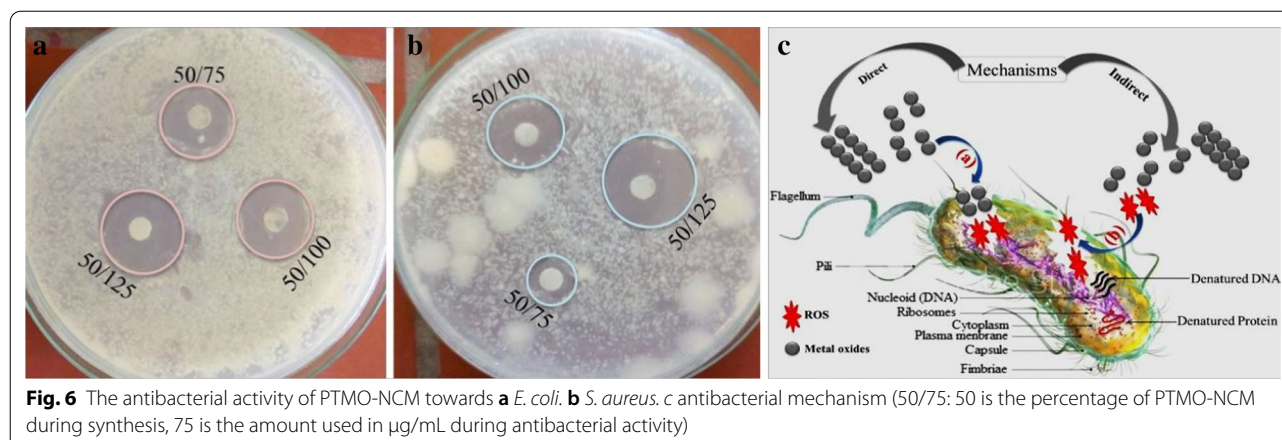
The band edge position of metal oxides is highly dependent on the surface charge. For effective photocatalytic reaction, the bottom of the CB needs to be more negative than the redox potential of H^+/H_2 and the top of the VB needs to be more positive than the redox potential of O_2/H_2O [40, 41]. As reported [13], the CB of Mn_2O_3 and ZnO is close to each other. Besides, for confirming the presence of an appropriate heterojunction and reality of the proper charge transfer synergy, analysis using electrochemical techniques such as CV and EIS is significant [42]. As seen in the CV (Fig. 1e) and EIS (Fig. 1f) analysis, the PTMO-NCM is showing the presence of a suitable heterojunction. Therefore, the possible photocatalytic mechanism was proposed as seen in Fig. 4e. During heterojunction, until the Fermi level equalizes, the energy band of metal oxides starts to move up and down by transferring electrons [8, 43] and lead to the creation of a depletion layer in the interface [44]. The Fermi level of p-type Mn_2O_3 exists near the VB. During UV irradiation, the photogenerated electrons have the probability of either localizing on the ZnO CB or diffusing to the VB of the Mn_2O_3, and the holes move to the VB of Fe_2O_3. Therefore, the recombination of the electrons and holes diminished and resulted in enhanced photocatalytic activity [8].

From the CV graph of PTMO-NCM (Fig. 5a), the reduction-reaction peaks were observed. As reported [45], this fast and reversible redox reaction is indicated to be due to the porous nature of the materials. This is also consistent with the BET and SEM characterization results. The obtained approximate peak potential difference ($\Delta E_{a,c}$) between E_{pa} (+ 0.401 V) and E_{pc} (+ 0.323 V) peak is 0.078 V. This smaller $\Delta E_{a,c}$ value shows the capability of the PTMO-NCM material to be more reversible. With an increase in the scan rate, the redox peaks positively shifted towards anodic and cathodic potentials. As seen in Fig. 5b CV plot and Fig. 5c amperometry plot, the novelty of the PTMO-NCM as an ascorbic acid sensor was also confirmed, as the concentration of ascorbic acid increase results in increasing the current rise. The sensing nobility of the material was also confirmed from the amperometry analysis as the sensing cycle was completed within a few seconds. The cycles were repeated to evaluate the stability of the electrode for 1 h. The obtained result confirms the stability and reproducibility of the PTMO-NCM electrode.

The antibacterial activity of metal oxides is highly dependent on the particle size [46] and ROS [47] generation capacities of the materials. By taking different precursor percentages and PVA polymer amount [26], the optimum antibacterial activities of PTMO-NCM towards *E. coli* and *S. aureus* (Fig. 6a, b, respectively) were determined to be 50% ZnO, 25% Fe_2O_3, and 25% Mn_2O_3. The enhanced antibacterial activities for PTMO-NCM were achieved compared to both single ZnO- and binary ZnO-based materials [27]. The antimicrobial activity mechanism of NPs may follow three mechanisms [48], including the release of antimicrobial ions [25, 49], the interaction of NPs with microorganisms [50], and the formation of ROS by the effect of light radiation [51]. As confirmed from the XRD pattern and UV–Vis-DRS spectra, the structural distortion and band position shift had not observed. The absence of this distortion and shift is due to the non-intercalation of Fe^{3+}/Mn^{3+} ions. This indicates the antimicrobial activity due to ions may not be the proper mechanism.

Fig. 5 **a** CV plots at different scan rates. **b** CV ascorbic acid sensing curve at different concentrations. **c** Amperometric ascorbic acid sensing plot at different concentrations

Fig. 6 The antibacterial activity of PTMO-NCM towards **a** *E. coli*. **b** *S. aureus*. *c* antibacterial mechanism (50/75: 50 is the percentage of PTMO-NCM during synthesis, 75 is the amount used in μg/mL during antibacterial activity)

Therefore, the direct and indirect ways of ROS generation [52] were proposed as an antibacterial activities mechanism, as seen in Fig. 6c.

Conclusions

The PTMO-NCM that has high porosity, enhanced surface area, and superior charge transfer capability was synthesized using the sol–gel followed by self-propagation techniques. Using the XRD pattern and TEM image analysis, the approximate average crystalline size of PTMO-NCM was determined to be in the range of 10–60 nm. The crystalline size of PTMO-NCM is six times smaller than bare ZnO. Compared to ZnO, fifteen times surface area enhancement for PTMO-NCM was confirmed from BET analysis. The less crystalline nature of the PTMO-NCM further confirmed from the stacking faults present on the HRTEM (IFFT) image and the absence of diffraction spots on the SAED ring. The nine times smaller semicircular diameter on the EIS and an enhanced current rise on CV indicate the presence of novel charge transfer properties for PTMO-NCM, compared to ZnO. From the adsorption kinetics and adsorption isotherms study, the adsorbate–adsorbent interaction was examined to be a chemisorption type. From the Langmuir model, the maximum adsorption capacity was determined to be 7.75 mg g^{-1}. The photocatalytic equilibrium constants were found to be 0.007141 min^{-1} and 0.005627 min^{-1} for CR and AO8 dyes, respectively. The superior sensing capability and noble antibacterial activities of PTMO-NCM were also verified.

Supplementary Information

The online version contains supplementary material available at https://doi.org/10.1186/s11671-020-03464-0.

Additional file 1: 1. Reagents. **2.** Materials and Instrumental details. **Figure S1.** a DRS-UV-vis. b direct Kubelka–Munk (Inset b: the respective indirect plots). c FT-IR spectra. **Figure S2.** EDX spectra (inset elemental percentage compositions).

Abbreviations

PTMO-NCM: Porous ternary metal oxide nanocomposite material; UV–Vis-DRS: UV–Vis-diffuse reflectance spectroscopy; FT-IR: Fourier transform infrared spectroscopy; XRD: X-ray powder diffraction; SEM: Scanning electron microscopy; EDX: Energy-dispersive X-ray spectroscopy; TEM: Transmission electron microscopy; HRTEM: High-resolution transmission electron microscopy; SAED: Selected area electron diffraction; BET: Brunauer–Emmett–Teller; CV: Cyclic voltammetry; EIS: Electrical impedance spectroscopy; FH: Flory–Huggins; FG: Fowler–Guggenheim; PFO: Pseudo-first-order; PSO: Pseudo-second-order; IPD: Intraparticle diffusion; CR: Congo red; AO8: Acid Orange-8; IFFT: Inverse fast Fourier transmission; ROS: Reactive oxygen species; *S. aureus*: *Staphylococcus aureus*; *E. coli*: *Escherichia coli*.

Authors' contributions
BA developed the idea and wrote this manuscript. Write up improvement and advising were performed by HCAM and EAZ. All authors read and approved the final manuscript.

Availability of data and materials
The datasets used and/or analyzed during the current study are available from the corresponding author on reasonable request.

Competing interests
The authors declare that they have no competing interests.

References

1. Abebe B, H C AM, Zerefa E, Abdisa E, (2020) Porous PVA/Zn–Fe–Mn oxide nanocomposites: methylene blue dye adsorption studies. Mater Res Express 7:065002. https://doi.org/10.1088/2053-1591/ab94fc
2. Abebe B, Murthy HA, Amare E (2020) Enhancing the photocatalytic efficiency of ZnO: defects, heterojunction, and optimization. Environ Nanotechnol Monit Manag 14:100336. https://doi.org/10.1016/j.enmm.2020.100336
3. Balati A, Tek S, Nash K, Shipley H (2019) Nanoarchitecture of TiO_2 microspheres with expanded lattice interlayers and its heterojunction to the laser modified black TiO_2 using pulsed laser ablation in liquid with improved photocatalytic performance under visible light irradiation. J Colloid Interface Sci 541:234–248. https://doi.org/10.1016/j.jcis.2019.01.082
4. Yemmireddy VK, Hung Y-C (2017) Using photocatalyst metal oxides as antimicrobial surface coatings to ensure food safety-opportunities and challenges. Compr Rev Food Sci Food Saf 16:617–631. https://doi.org/10.1111/1541-4337.12267
5. Ibupoto ZH, Shah SMUA, Khun K, Willander M (2012) Electrochemical L-lactic acid sensor based on immobilized ZnO nanorods with lactate oxidase. Sensors 12:2456–2466. https://doi.org/10.3390/s120302456
6. Janotti A, Van de Walle CG (2009) Fundamentals of zinc oxide as a semiconductor. Rep Prog Phys 72:126501. https://doi.org/10.1088/0034-4885/72/12/126501
7. Akkari M, Aranda P, Belver C et al (2018) ZnO/sepiolite heterostructured materials for solar photocatalytic degradation of pharmaceuticals in wastewater. Appl Clay Sci 156:104–109. https://doi.org/10.1016/j.clay.2018.01.021
8. Lachheb H, Ajala F, Hamrouni A et al (2017) Electron transfer in ZnO–Fe_2O_3 aqueous slurry systems and its effects on visible light photocatalytic activity. Catal Sci Technol 7:4041–4047. https://doi.org/10.1039/C7CY01085K
9. Jassby D, Farner Budarz J, Wiesner M (2012) Impact of aggregate size and structure on the photocatalytic properties of TiO_2 and ZnO nanoparticles. Environ Sci Technol 46:6934–6941. https://doi.org/10.1021/es202009h
10. Balati A, Wagle D, Nash KL, Shipley HJ (2019) Heterojunction of TiO_2 nanoparticle embedded into ZSM5 to 2D and 3D layered-structures of MoS_2 nanosheets fabricated by pulsed laser ablation and microwave technique in deionized water: structurally enhanced photocatalytic performance. Appl Nanosci 9:19–32. https://doi.org/10.1007/s13204-018-0902-x
11. Balati A, Matta A, Nash K, Shipley HJ (2020) Heterojunction of vertically aligned MoS_2 layers to hydrogenated black TiO_2 and rutile based inorganic hollow microspheres for the highly enhanced visible light arsenic photooxidation. Compos B Eng 185:107785. https://doi.org/10.1016/j.compositesb.2020.107785
12. Balati A, Bazilio A, Shahriar A et al (2019) Simultaneous formation of ultra-thin $MoSe_2$ nanosheets, inorganic fullerene-like $MoSe_2$ and MoO_3 quantum dots using fast and ecofriendly pulsed laser ablation in liquid followed by microwave treatment. Mater Sci Semicond Process 99:68–77. https://doi.org/10.1016/j.mssp.2019.04.017
13. Saravanan R, Gupta VK, Narayanan V, Stephen A (2014) Visible light degradation of textile effluent using novel catalyst ZnO/γ-Mn_2O_3. J Taiwan Inst Chem Eng 45:1910–1917. https://doi.org/10.1016/j.jtice.2013.12.021
14. Hashim FS, Alkaim AF, Mahdi SM, Omran Alkhayatt AH (2019) Photocatalytic degradation of GRL dye from aqueous solutions in the presence of ZnO/Fe_2O_3 nanocomposites. Compos Commun 16:111–116. https://doi.org/10.1016/j.coco.2019.09.008
15. Ali DA, El-Katori EE, Kasim EA (2019) Sol–gel sonochemical triton X-100 templated synthesis of Fe_2O_3/ZnO nanocomposites toward developing photocatalytic degradation of organic pollutants. Z Phys Chem. https://doi.org/10.1515/zpch-2019-1518
16. Saravanan R, Khan MM, Gupta VK et al (2015) ZnO/Ag/Mn_2O_3 nanocomposite for visible light-induced industrial textile effluent degradation, uric acid and ascorbic acid sensing and antimicrobial activity. RSC Adv 5:34645–34651. https://doi.org/10.1039/C5RA02557E
17. Wu Z, Wu W (2015) Shape control of inorganic nanoparticles from solution. Nanoscale 8:1237–1259. https://doi.org/10.1039/c5nr07681a
18. Kumar S, Krishnakumar B, Sobral AJFN, Koh J (2019) Bio-based (chitosan/PVA/ZnO) nanocomposites film: thermally stable and photoluminescence material for removal of organic dye. Carbohydr Polym 205:559–564. https://doi.org/10.1016/j.carbpol.2018.10.108
19. Radhamani AV, Shareef KM, Rao MSR (2016) ZnO@MnO_2 core–shell nanofiber cathodes for high performance asymmetric supercapacitors. ACS Appl Mater Interfaces 8:30531–30542. https://doi.org/10.1021/acsami.6b08082
20. Liu Y, Pang H, Wei C et al (2014) Mesoporous ZnO–NiO architectures for use in a high-performance nonenzymatic glucose sensor. Microchim Acta 181:1581–1589. https://doi.org/10.1007/s00604-014-1275-9
21. Khan SB, Ahmed MS, Asiri AM (2016) Amperometric sensor for ascorbic acid using a gold electrode modified with ZnO@SiO_2 nanospheres. New J Chem 40:8438–8443. https://doi.org/10.1039/C6NJ00115G
22. Rice ME (2000) Ascorbate regulation and its neuroprotective role in the brain. Trends Neurosci 23:209–216. https://doi.org/10.1016/S0166-2236(99)01543-X
23. Weldegebrieal GK (2020) Synthesis method, antibacterial and photocatalytic activity of ZnO nanoparticles for azo dyes in wastewater treatment: a review. Inorg Chem Commun 120:108140. https://doi.org/10.1016/j.inoche.2020.108140
24. Ozkan E, Ozkan FT, Allan E, Parkin IP (2015) The use of zinc oxide nanoparticles to enhance the antibacterial properties of light-activated polydimethylsiloxane containing crystal violet. RSC Adv 5:8806–8813. https://doi.org/10.1039/c4ra13649g
25. Espitia PJP, Soares NFF, Coimbra JSR et al (2012) Zinc oxide nanoparticles: synthesis, antimicrobial activity and food packaging applications. Food Bioprocess Technol 5:1447–1464. https://doi.org/10.1007/s11947-012-0797-6
26. Abebe B, Murthy HCA, Zerefa E, Adimasu Y (2020) PVA assisted ZnO based mesoporous ternary metal oxides nanomaterials: synthesis, optimization, and evaluation of antibacterial activity. Mater Res Express 7:045011. https://doi.org/10.1088/2053-1591/ab87d5
27. Abebe B, Murthy HCA, Zereffa EA, Adimasu Y (2020) Synthesis and characterization of ZnO/PVA nanocomposites for antibacterial and electrochemical applications. Inorg Nano-Metal Chem. https://doi.org/10.1080/24701556.2020.1814338
28. Abebe B, Murthy HCA, Zereffa EA, Qiang Y (2020) Synthesis and characterization of PVA-assisted metal oxide nanomaterials: surface area, porosity, and electrochemical property improvement. J Nanomater 2020:1–14. https://doi.org/10.1155/2020/6532835
29. Makuła P, Pacia M, Macyk W (2018) How to correctly determine the band gap energy of modified semiconductor photocatalysts based on UV–Vis spectra. J Phys Chem Lett 9:6814–6817. https://doi.org/10.1021/acs.jpclett.8b02892
30. Tallapally V, Nakagawara TA, Demchenko DO et al (2018) $Ge_{1-x}Sn_x$ alloy quantum dots with composition-tunable energy gaps and near-infrared photoluminescence. Nanoscale 10:20296–20305. https://doi.org/10.1039/C8NR04399J
31. Zeng Z, Zhang W, Arvapalli DM et al (2017) A fluorescence-electrochemical study of carbon nanodots (CNDs) in bio- and photoelectronic applications and energy gap investigation. Phys Chem Chem Phys 19:20101–20109. https://doi.org/10.1039/C7CP02875J
32. Muñoz-Rojas D, Oró-Solé J, Gómez-Romero P (2008) From nanosnakes to nanosheets: a matrix-mediated shape evolution. J Phys Chem C 112:20312–20318. https://doi.org/10.1021/jp808187w
33. Tallapally V, Damma D, Darmakkolla SR (2019) Facile synthesis of size-tunable tin arsenide nanocrystals. Chem Commun 55:1560–1563. https://doi.org/10.1039/C8CC08101H
34. Borchert H, Shevchenko EV, Robert A et al (2005) Determination of nanocrystal sizes: a comparison of TEM, SAXS, and XRD studies of highly monodisperse $CoPt_3$ particles. Langmuir 21:1931–1936. https://doi.org/10.1021/la0477183
35. Thommes M, Kaneko K, Neimark AV et al (2015) Physisorption of gases, with special reference to the evaluation of surface area and pore size distribution (IUPAC Technical Report). Pure Appl Chem 87:1051–1069. https://doi.org/10.1515/pac-2014-1117

Abebe *et al. Nanoscale Res Lett*   (2021) 16:1

Page 9 of 9

36. Gopinathan E, Viruthagiri G, Shanmugam N, Sathiya priya S (2015) Optical, surface analysis and antibacterial activity of ZnO–CuO doped cerium oxide nanoparticles. Optik (Stuttg) 126:5830–5835. https://doi.org/10.1016/j.ijleo.2015.09.014

37. Li Z, Mi Y, Liu X et al (2011) Flexible graphene/MnO_2 composite papers for supercapacitor electrodes. J Mater Chem 21:14706. https://doi.org/10.1039/c1jm11941a

38. Zhai T, Xie S, Zhao Y et al (2012) Controllable synthesis of hierarchical ZnO nanodisks for highly photocatalytic activity. CrystEngComm 14:1850. https://doi.org/10.1039/c1ce06013a

39. Edet UA, Ifelebuegu AO (2020) Kinetics, isotherms, and thermodynamic modeling of the adsorption of phosphates from model wastewater using recycled brick waste. Processes 8:665. https://doi.org/10.3390/pr8060665

40. Hoffmann MR, Martin ST, Choi W, Bahnemann DW (1995) Environmental applications of semiconductor photocatalysis. Chem Rev 95:69–96. https://doi.org/10.1021/cr00033a004

41. Mills A, Le Hunte S (1997) An overview of semiconductor photocatalysis. J Photochem Photobiol A Chem 108:1–35. https://doi.org/10.1016/S1010-6030(97)00118-4

42. Beranek R (2011) (Photo)electrochemical methods for the determination of the band edge positions of TiO_2-based nanomaterials. Adv Phys Chem 2011:1–20. https://doi.org/10.1155/2011/786759

43. Tama AM, Das S, Dutta S et al (2019) MoS_2 nanosheet incorporated α-Fe_2O_3/ZnO nanocomposite with enhanced photocatalytic dye degradation and hydrogen production ability. RSC Adv 9:40357–40367. https://doi.org/10.1039/C9RA07526G

44. Zhang J, Liu X, Wang L et al (2011) Synthesis and gas sensing properties of α-Fe_2O_3@ZnO core–shell nanospindles. Nanotechnology 22:185501. https://doi.org/10.1088/0957-4484/22/18/185501

45. Liu J, Xu T, Sun X et al (2019) Preparation of stable composite porous nanofibers carried SnO_x–ZnO as a flexible supercapacitor material with excellent electrochemical and cycling performance. J Alloys Compd 807:151652. https://doi.org/10.1016/j.jallcom.2019.151652

46. Raghupathi KR, Koodali RT, Manna AC (2011) Size-dependent bacterial growth inhibition and mechanism of antibacterial activity of zinc oxide nanoparticles. Langmuir 27:4020–4028. https://doi.org/10.1021/la104825u

47. Nair S, Sasidharan A, Divya Rani VV et al (2009) Role of size scale of ZnO nanoparticles and microparticles on toxicity toward bacteria and osteoblast cancer cells. J Mater Sci Mater Med 20:235–241. https://doi.org/10.1007/s10856-008-3548-5

48. Abebe B, Zereffa EA, Tadesse A, Murthy HCA (2020) A review on enhancing the antibacterial activity of ZnO: mechanisms and microscopic investigation. Nanoscale Res Lett 15:190. https://doi.org/10.1186/s11671-020-03418-6

49. Kasemets K, Ivask A, Dubourguier H-C, Kahru A (2009) Toxicity of nanoparticles of ZnO, CuO and TiO_2 to yeast *Saccharomyces cerevisiae*. Toxicol Vitr 23:1116–1122. https://doi.org/10.1016/j.tiv.2009.05.015

50. Zhang L, Ding Y, Povey M, York D (2008) ZnO nanofluids—a potential antibacterial agent. Prog Nat Sci 18:939–944. https://doi.org/10.1016/j.pnsc.2008.01.026

51. Jalal R, Goharshadi EK, Abareshi M et al (2010) ZnO nanofluids: green synthesis, characterization, and antibacterial activity. Mater Chem Phys 121:198–201. https://doi.org/10.1016/j.matchemphys.2010.01.020

52. Thakur N, Manna P, Das J (2019) Synthesis and biomedical applications of nanoceria, a redox active nanoparticle. J Nanobiotechnology 17:84. https://doi.org/10.1186/s12951-019-0516-9

Publisher's Note